Article:
Escalona, M., Bhuyan, Heman, Valenzuela, J.C. et al. (6 more authors) (2021) Comparative study on the dynamics and the composition between a pulsed laser deposition (PLD) and a plasma enhanced PLD (PE-PLD). Results in Physics. 104066. ISSN 2211-3797

https://doi.org/10.1016/j.rinp.2021.104066

Comparative study on the dynamics and the composition between a pulsed laser deposition (PLD) and a plasma enhanced PLD (PE-PLD).

M. Escalona[1], H. Bhuyan[1,2,*], J.C. Valenzuela[1], S. Ibacache[1], E. Wyndham[1], M. Favre[1,2], F. Veloso[1,2], H.M. Ruiz[3], and E. Wagenaars[4].

[1] Institute of Physics, Pontificia Universidad Católica de Chile, Av. Vicuña Mackenna 4860, Santiago, Chile

[2] Centro de Investigación en Nanotecnología y Materiales Avanzados (CIEN-UC), Av. Vicuña Mackenna 4860, Santiago, Chile.

[3] Departamento de Física, Universidad Técnica Federico Santa María, Av. España, 1680 Valparaíso, Chile

[4] York Plasma Institute, Department of Physics, University of York, York YO10 5DD, UK

Abstract

We report the effect of single and dual radio frequency (RF) plasma discharge on the composition and dynamics of a titanium plasma plume produced in a plasma-enhanced pulsed laser deposition (PE-PLD) system. The study was carried out in a nitrogen environment at different pressures. Time-resolved images, optical emission spectroscopy, and interferometry were employed to analyze the plasma. We were able to fit time-resolved images using different expansion models, obtained an expansion velocity between 6 and 30 x 10^3 m/s. Emission lines from N II, Ti II, were observed by changing the pressure and RF conditions. An increase in emission line intensity from N II was observed by increasing the pressure and RF power. We used Ti II lines to estimate the plasma temperature by using the Boltzmann equation, and we obtained the density from the Ti II line (454.9 nm) through Stark broadening. In addition, a Mach-Zehnder interferometer was employed to make a two-dimensional map of the electron density at early times. The estimated temperatures and densities are between 0.8 - 2.0 eV and 10^{17} – 10^{18} cm^{-3}, respectively. The results suggest that increasing RF power enhanced the Ti-N atoms interaction, which is crucial in titanium nitride film applications.

Keywords: Titanium nitride, plasma-enhanced pulsed laser deposition, dual radio-frequency plasma, thin film, optical spectroscopy, interferometry.

*hbhuyan@fis.puc.cl

1. Introduction

Titanium is widely used in industrial applications where its high resistance to heat and corrosion is valued. Furthermore, titanium may be combined with other elements to produce new materials with superior properties in a wide application range. For example, titanium nitride (TiN) is widely employed in semiconductor manufacturing, selective transparent film, high-performance cutting, biocompatible surface, forming tools, and thermal barriers in nuclear fusion and chemical reactors. These applications rely on a wide range of distinctive properties, including hardness, high melting point, high electrical conductivity, and tribological affinity [1-7].

There have been many investigations on the growth of Ti thin films using different modern techniques such as magnetron plasma [8], plasma ion implantation [9], physical vapor deposition [10], chemical vapor deposition [11], and Pulsed Laser Deposition (PLD) [12]. In particular, PLD provides several advantages for depositing thin films compared to the other techniques; the most relevant are a) high stoichiometric reproducibility from the material target into the film. b) Atoms and ions have high kinetic energy when arriving at the substrate, which improves the sticking and superficial mobility, allowing deposition with less temperature than other techniques and c) the thickness can be easily controlled by the number of pulses or laser fluence [13, 14]. However, PLD also has some disadvantages; for example, only a small area and few samples can be deposited at a time since the plasma volume limits effective area. To overcome this, several authors have used a laser scanning unit to move the plasma plume to cover more area, achieving a homogeneous deposit of surfaces up to 200 mm in diameter [15, 16]. Another challenge is that the PLD technique limits the absorption of atoms from the background gas due to the working gas's reactivity level and collisionality. The use of an external/background plasma environment has shown potential benefits in terms of the film quality and the deposition rate due to the increased plasma reactivity with the laser-ablated molecules [17-20]. The combination is termed as plasma-enhanced PLD (PE-PLD). However, most of the studies on PE-PLD merely focus on studying changes in the deposited films without characterizing the interaction between the laser-produces plasma and the RF plasma. Research of the plasma can play a crucial role in the process of optimizing and controlling the thin films, since knowing plasma parameters, together with the dynamics and composition, it is possible to make correlations with the properties of the grown films.

Moreover the emission of energetic ions during laser ablation aids reactive species formation, permitting better adhesion to the substrate and growth of epitaxial films at low temperatures [21].

Here we report a study on the physics behind the use of capacitive coupled dual RF plasma as a background medium to the PLD. The novelty of this work is that we used a dual radio frequency reactor to create the PE-PLD configuration. In this way we add two additional parameters: the source RF power and the frequencies. Both parameters are important as they allow the interaction between the plasma regions present. The reason is that for dual capacitive coupled plasmas, the capacitive sheath is thicker at lower frequencies and provides great impedance to the low frequency current. Consequently, by tuning the low frequency (LF) power, it is possible to control the high energy ion bombardment at the powered electrode. In contrast, at higher frequencies, the sheath is thinner and provides a lower value of the impedance to the high frequency (HF) current and permits a greater flow of HF currents, which leads to enhanced plasma ionization. By these means, the tuning of the HF power can control the plasma density and the ion flux at the powered electrode [22].

In this work we compare the plasma parameters, dynamics, and composition for both PLD and PE-PLD configurations. As a result we are able to contribute to the improvement and understanding of the growth of TiN films in a PE-PLD system, by reporting and discussing differences in the expansion of titanium plasma in a nitrogen environment. We use optical emission spectroscopy to identify excited species of titanium plasma and their interaction with the background gas. The electron temperature T_e and the density N_e are determined from the relative ionic line intensity measurements using a Boltzmann plot and Stark broadening, respectively. The dynamics of the shock wave are observed using fast photography. In addition, interferometry is used at early times to complement the density measurements made by Stark broadening of the titanium plasma and to determine the initial density of the plasma plume and the shock wave.

2. Experimental setup

The experiment setup is shown in Figure 1. The experiments were performed in a stainless-steel vacuum chamber at a base pressure of 0.05 mTorr. Laser 1 is used to ablate titanium from a pure titanium target. Laser 1 is a Nd:YAG pulsed laser at 1064 nm with a 4.8 ns full

width half maximum (FWHM) operated at 10 Hz repetition rate and provide 200 mJ/pulsed laser energy to the target. The target is rotated between shots and the laser has an orientation approximately 60° off normal. The Laser spot on the target is elliptical with an area of 1.57 mm^2 and the resulting fluence is 12.74 J/cm^2 with a power density of 2.65 GW/cm^2. The ablation of titanium is performed in a nitrogen atmosphere in the pressure range of 10-1000 mTorr. The PLD setup is enhanced by generating RF plasma in an asymmetric capacitive coupled configuration. Detailed description may be found elsewhere [23, 24]. The chamber has an inner diameter of 40 cm and a height of 35.7 cm. Two stainless steel plates (AISI 314) form plane-parallel electrodes, between which the plasma is generated. The upper electrode has a diameter of 10 cm and is grounded. The lower electrode (powered electrode) has a diameter of 8 cm and is connected to two RF generators, at 2.26 MHz (LF) and 13.56 MHz (HF) via a combination of impedance matching networks. The powered electrode is surrounded by a solid polyethylene bar. The HF generator is an ENI ACG-6B and the LF generator is a Barthel RFG-2–300-L. These have a maximum power of 600 W and 300W, respectively. The automatic matching networks (ENI MWH-5–01 and MCi-2–300) maximize the power delivered to the plasma. In each RF generator a filter blocks the return path of undesired frequencies.

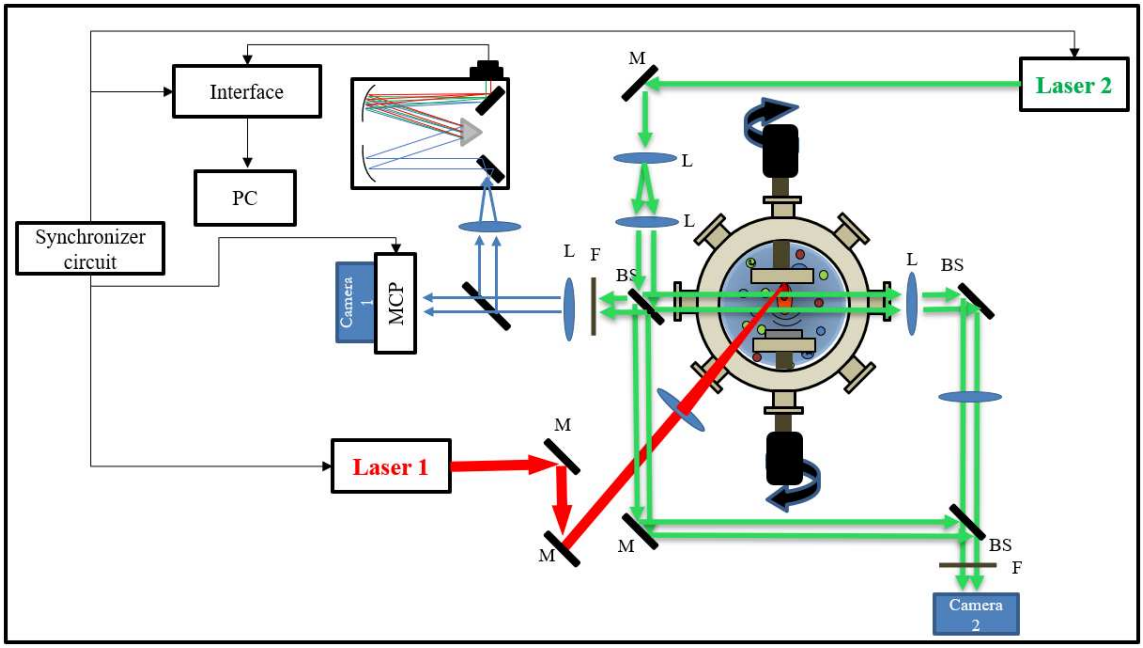

Figure 1. Experimental Setup of PE-PLD system with the diagnostic systems.

We used three experimental techniques to study the physics of PLD and PE-PLD systems at different pressures and RF conditions. First, in order to observe the plasma evolution images of the emission of the expanding plasma plume were obtained using a gated microchannel plate (MCP) camera, with a resolution of 15 ns (Camera 1), over a range of times with respect to the laser ablation pulse. Second, time-resolved optical spectra of the plasma emission are observed 5 mm from the target surface using a lens-fiber optic system, with a spatial resolution of 4 mm. The emission is resolved with a Spectra Pro 275 (1200 g/mm) spectrometer. The detection system consist of 512 diodes array (model 1455 EG&G Princeton Applied Research) with a gating interval of 15 ns. The entire system is calibrated for wavelength and intensity. Third, the plasma density profiles are measured with a Mach-Zehnder interferometer using a second laser (Laser 2, 4 ns FWHM at 532 nm). A bandpass interference filter is placed in front of the camera (Camera 2) to select the laser wavelength.

3. Results and discussion

3.1.Time-resolved images

The images of the plasma self-emission show the expansion of the plasma. The images in Figure 2 show the titanium plasma expansion at different nitrogen background pressures.

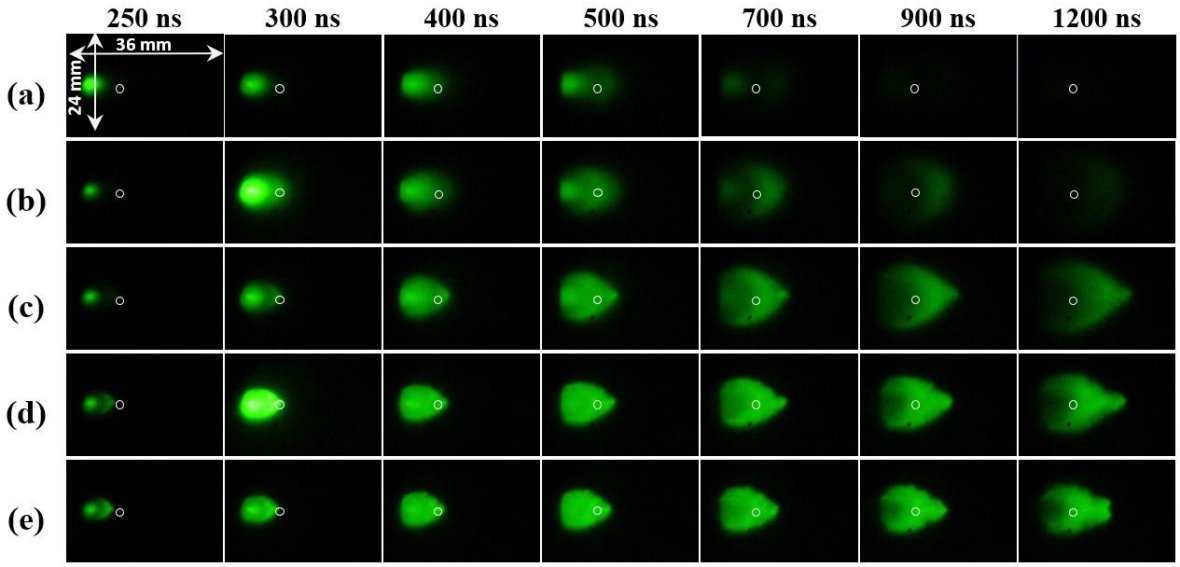

Figure 2. Time-resolved images of plasma expansion at different nitrogen pressure: a) 10 mTorr, b) 50 mTorr, c) 130 mTorr, d) 500 mTorr and e) 1 Torr. White circle represents the region where the spectra are acquired.

The evolution of the plasma structure is seen to be pressure dependent: At 10 mTorr, the lifetime of the plasma plume is short, and the expansion is essentially perpendicular to the target surface due to the long mean free path. At 50 mTorr, the interaction with the background gas becomes significant, and the plume front tends towards spherical geometry. It is also visible for longer. At 130 mTorr, the extent of the plasma plume is greatest and its front becomes sharpened. At 500 mTorr and 1 Torr, the intensity of the plume increases, as does its lifetime. However the size of the plasma plume decreases and distortions or fine structures in the shock front are distinguished after 400 ns.

The sharp pointed plume in a PLD system has been reported in an aluminum plasma [25,26]. The sharp nature was attributed to the fact that ions with a higher charge state dominate in the direction normal to the target. Therefore, in the initial state, when electrons are ejected, a space charge field accelerates the ions, causing the ions with a higher charge state to be faster. The sharp pointed plume has also been reported in plasma produced by femtosecond laser where the higher kinetic energy components travel in a direction normal to the target, with their densities falling in the radial direction [27].

The images of the plasma plume can be used to understand the processes of the plasma expansion. The position of the plasma front at different times (R-time plot) is shown in Figure 3. The wide range of pressures used requires the use of different models to cover the different regimes. At 10 mTorr, as shown in Figure 3a, a linear behavior is observed. This corresponds to the long mean free path (mfp) of the titanium plasma in the background gas. Here, the model supposes the interaction of smooth rigid elastic spherical molecules [28]. In the case of nitrogen at 10 mTorr, the mfp is estimated to be 17 mm, which is close to the maximum visible extension of Figure 2a. Hence, we anticipate (near) free adiabatic expansion. However, at 50 mTorr, the mfp is approximately 3.5 mm. In which case, the interaction of the plasma plume with the neutral nitrogen background becomes appreciable. On increasing the pressure to 130 mTorr, the expansion is not even approximately linear. In this regime, the data is best fitted by the shock wave model, as can be seen in Figure 3b. This model assumes that the amount of background gas swept up becomes comparable to the initial mass of ejected material and the energy released in the ablation is much greater than the energy lost by radiation. The result is that the wave pressure is higher than the ambient

pressure [29]. The wavefront expansion is predicted using the shock wave model proposed by Taylor-Sedov:

$$R = \xi \left(\frac{E}{\rho}\right)^{1/(2+\beta)} t^{2/(2+\beta)} \quad . \qquad (1)$$

Here, E is the energy released during explosion, ρ is the ambient gas density, t is the delay time, β is a dependent parameter of the expansion geometry and has values of 1, 2, and 3 for the planar, cylindrical, and spherical cases. Finally, ξ is a constant which depends on the specific heat ratio γ and is given by: $\xi = \left[\left(\frac{75}{16\pi}\right)\frac{(\gamma-1)(\gamma+1)^2}{3\gamma-1}\right]^{1/5}$. At 50 mTorr and 130 mTorr, we observed that the exponent is estimated to be 0.60 and 0.57, respectively.

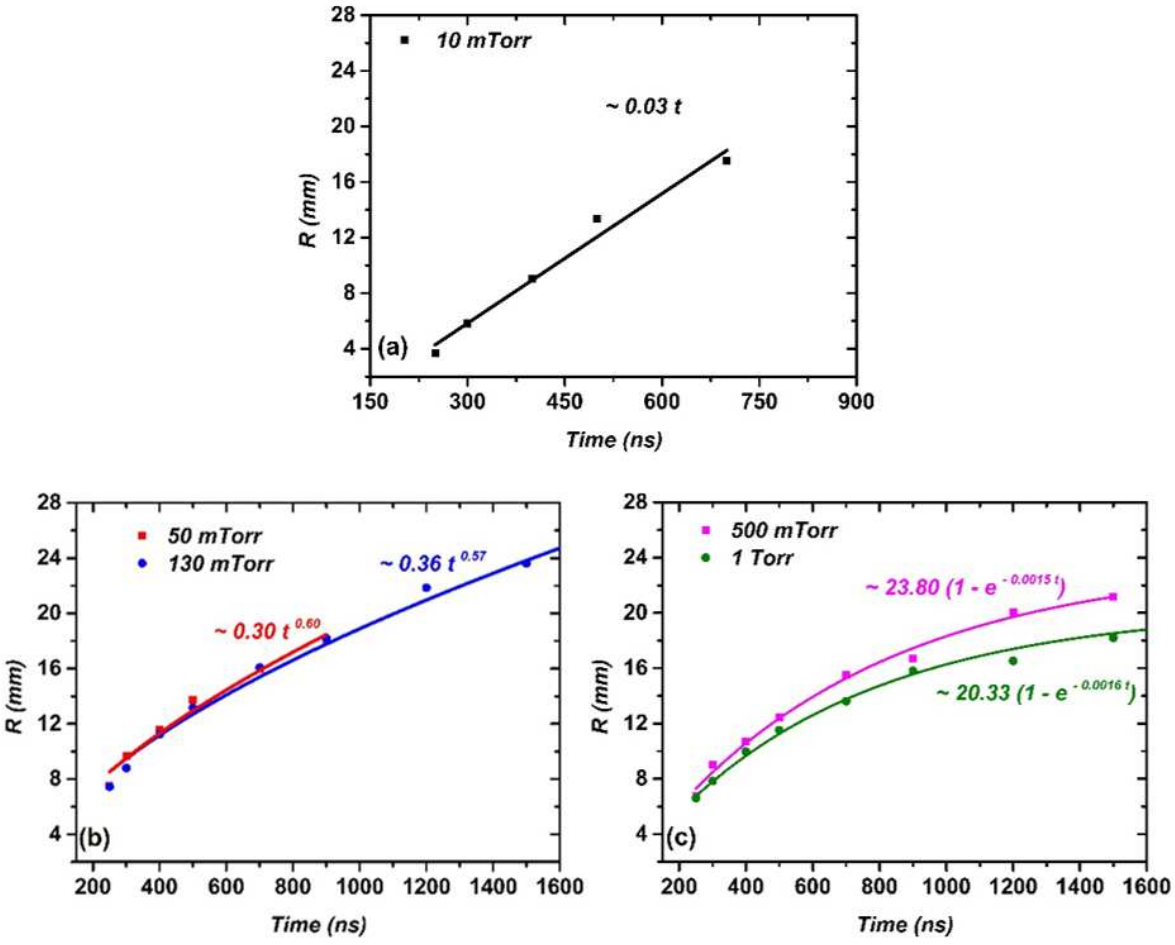

Figure 3. Temporal evolution of the plasma front is modeled at different nitrogen pressures. **a)** 10 mTorr using the free expansion model, **b)** 50 and 130 mTorr with the shock model and **c)** 500 mTorr and 1 Torr with the drag model.

At 500 mTorr and 1 Torr, the shock front is also pointed, but the visible intensity of the plume increases. We ascribe this to the increased interaction between the titanium plasma and the background. The confining effect on the plume, where increased collisionality allows the excited species to stay for longer, while at the same time the energy lost from radiation increases. Under these conditions, it is appropriate to apply the drag model. This may be seen in Figure 3c. In the drag model, viscosity is proportional to the velocity of ejected material, i.e. $dv/dt = -\beta v$, where β is called the stopping or drag coefficient [30]. The solution is given by

$$R = R_0(1 - e^{-\beta t}), \qquad (2)$$

where $R_0 = v_0/\beta$ is the stopping distance.

In addition we have compared the expansion behavior of the plume with and without the presence of RF power in the nitrogen environment. We ascribe this to the imaging method used, as it collects radiation from the plasma over a wide spectral range of 350–900 nm, making the method insensitive to specific wavelength changes. However, in the following section, we discuss the differences observed when using spectroscopy analysis.

3.2. Optical emission spectroscopy

The temporal evolution of the emission spectrum was observed at 5 mm from the target using a 15 ns temporal window. The nitrogen pressure was varied from 10 mTorr to 1 Torr and the RF power was provided in single and dual configuration mode at the same total power of 70 W. Figure 4a shows a representative time-resolved spectrum of titanium plasma ejected into 50 mTorr neutral nitrogen (no RF). We observed nitrogen lines between 20 and 100 ns. This suggests the existence of an initial or first front that is not detected in the image analysis due to its low intensity. Therefore, the self-emission images, described in the previous section, correspond principally to emissions from titanium. Several molecular bands (N_2) and a singly ionized nitrogen line (N II) are identified at 37 ns, as shown in Figure 4b. It should be noted here that the intensity of the N II line increases significantly in the presence of the nitrogen RF plasma, which we discuss in the following section. Titanium lines were observed from 200 ns onwards, which is in agreement with Figure 2. At later time, several transition lines from singly ionized titanium (Ti II) were identified from the NIST database [31]. These are shown in Figure 4c.

In order to study the variations of titanium and nitrogen ions, we plot in Figure 5 the temporal evolution of Ti II (454.9 nm) and N II (460.1 nm) emission lines for different values of pressure and RF configurations, in single and dual frequency mode. The intensities corresponds only to the plasma produced by the laser component since it is not possible to measure the RF plasma contribution for the acquisition time used (15 ns). With the RF applied, we observe that the RF power promotes the formation of N II ions. An increase in RF power increases N II emission intensity and allows its formation earlier than at lower powers. Moreover, we observe a higher N II emission intensity when using only the HF source, as seen in Figure 5a. In contrast, the opposite trend is observed in the case of titanium, where the intensity from Ti II line decreases on using HF source, as may be seen in Figure 5b. The increase in the N II line is attributed to the

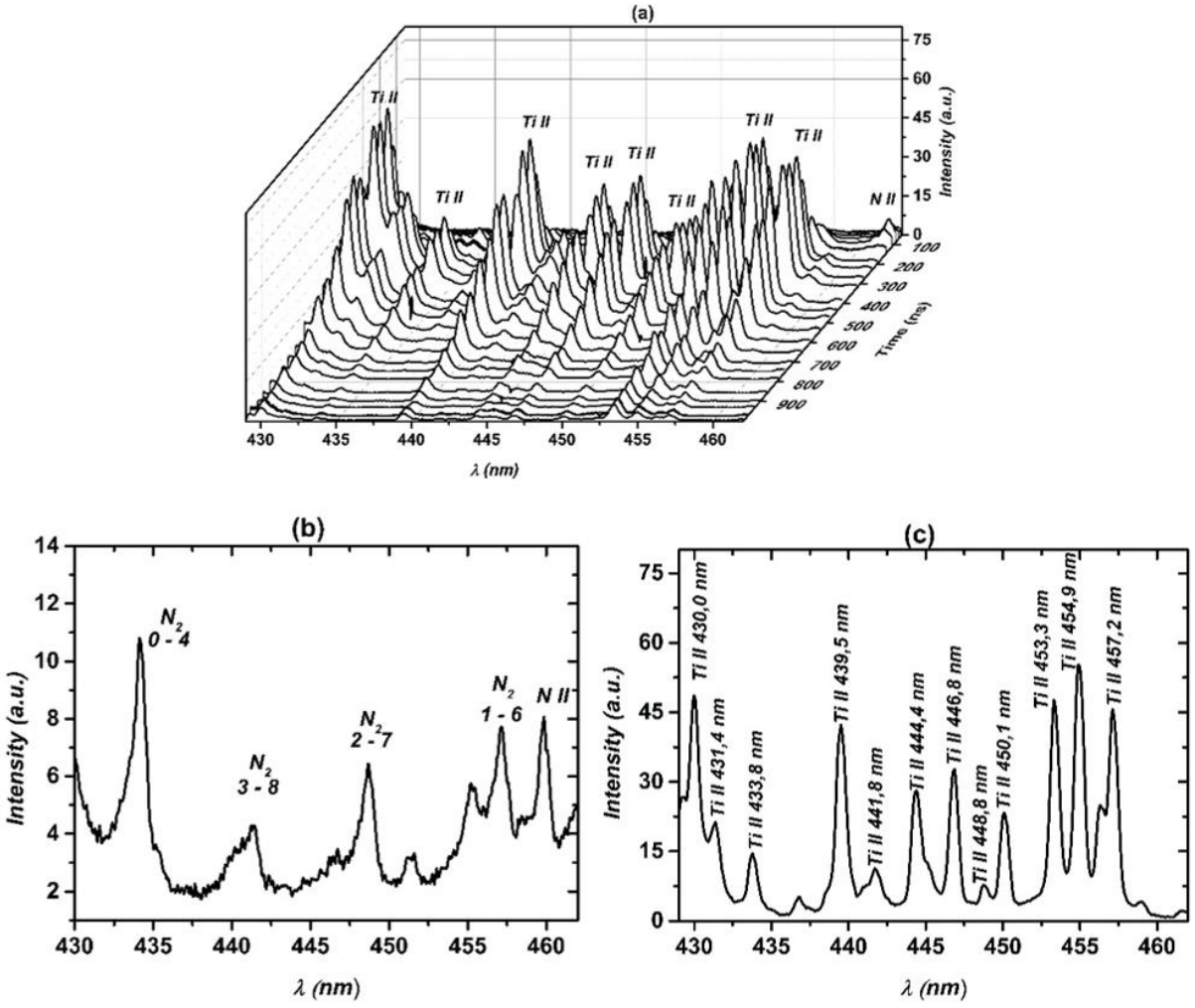

Figure 4. Optical emission spectrum at 50 mTorr neutral nitrogen, **a)** time resolved, **b)** 37 ns, and **c)** at 405 ns.

addition of RF energy, which improves probability of collision between electrons and atoms in the presence of HF power [32]. This increase in collisions allows the formation of more excited species that may in turn be ionized easily on interaction with the plume. In contrast, we anticipate that the decrease in Ti II may be due to recombination or transition to different energetic levels and the formation of TiN, whose emission lines are outside the range of wavelengths observed. We recall that on this point the influence of nitrogen plasma on the TiN film deposition was apparent in our previous study in the same PE-PLD system [33]. An increase in the nitrogen concentration and changes in the TiN film structure were observed on increasing RF power.

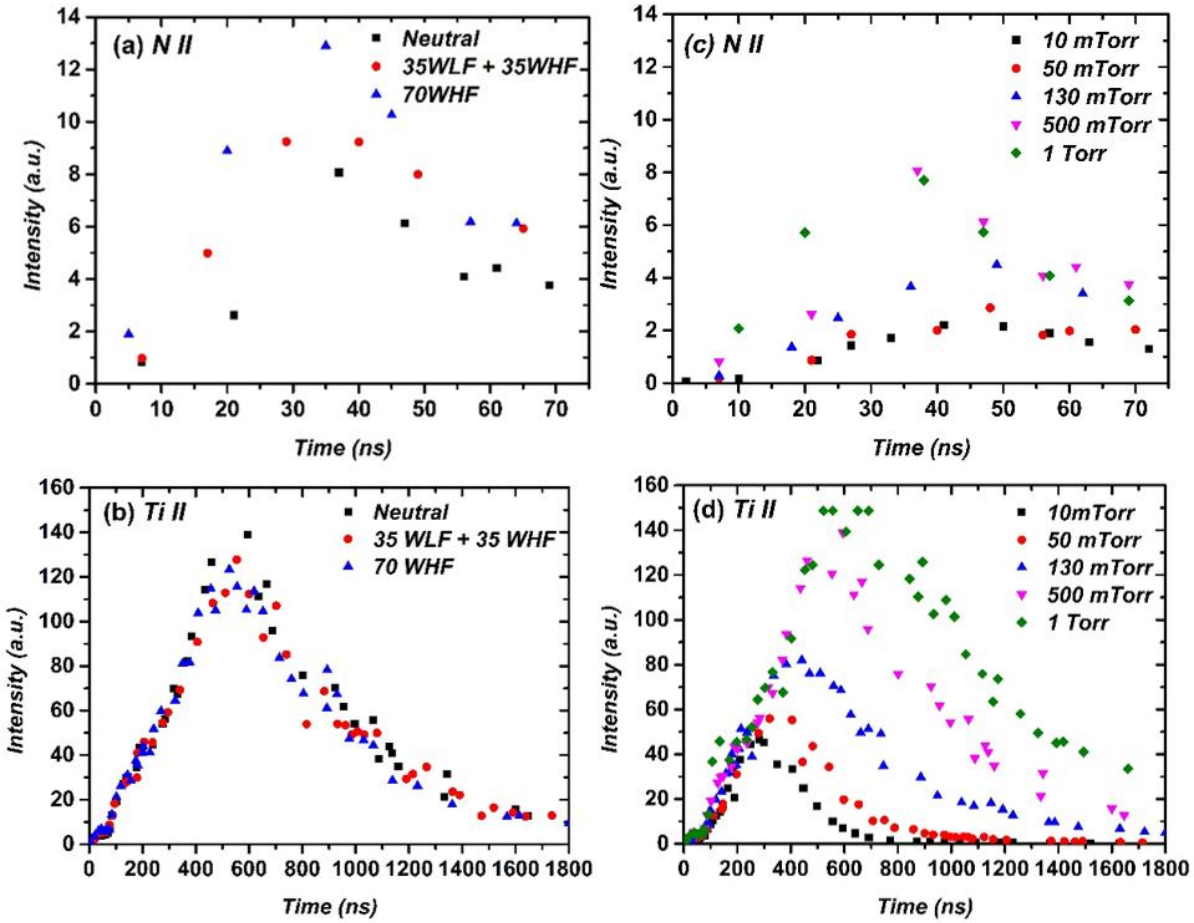

Figure 5. The temporal evolution of spectral intensity emission from **a)** N II (460.1 nm) and **b)** Ti II (454.9 nm) at different RF powers. In **c)** N II (460.1nm) and **d)** Ti II (454.9 nm) at different neutral pressures.

On the other hand, we observed an increase in the line intensity of N II and Ti II lines, with increasing pressure, as shown in Figures 5c and 5d. The increase in the intensity of Ti

II line is attributed to the fact that at higher pressure the effect of confinement mentioned above stimulates ionization from collisions, while the increase in the intensity of N II line is due to the laser intensity threshold for plasma initiation, which decreases with increasing pressure [34,35]. In consequence, the energy transferred from the laser and from the Ti plume to the background gas is more efficient in ionizing nitrogen. In addition, a shift in maximum intensity and longer lifetime is observed with increasing pressure as shown in Figure 5d, which we attribute to the effect of confinement observed from the analysis of the images in the previous section.

3.3.Electron temperature and density

Temperature and electron density were obtained assuming the plasma to be in local thermodynamic equilibrium (LTE). The validity of this assumption is considered later in this section. Under LTE, the Boltzmann method describes the population in excited energy levels as a function of temperature and electron density [36].

$$ln\left(\frac{I_{ki}\lambda_{ki}}{A_{ki}g_k}\right) = ln\left(\frac{N(T)}{U(T)}\right) - \frac{E_k}{kT} \qquad (3)$$

where I_{ki} is the intensity of the transition line from upper level (k) to a lower level (i), λ_{ki} is the wavelength, A_{ki} is the transition probability, g_k is the statistical weight, $N(T)$ is the density, $U(T)$ is the partition function, E_k is the energy of the upper level, k is the Boltzmann constant and T is the temperature to be determined. We use the relative intensities of eight lines of singly ionized titanium to plot $ln\left(\frac{I_{ki}\lambda_{ki}}{A_{ki}g_k}\right)$ vs. E_k, in which case the slope is $-\frac{E_k}{kT}$. The values of λ_{ki} , A_{ki}, g_k, and E_k were taken from the NIST database [31], which are listed in Table 1. Stark broadening describes the full width at half maximum ($\Delta\lambda_{1/2}$) of an emission line with the electronic density given by equation (4).

$$\Delta\lambda_{stark} = 2w\left(\frac{N_e}{10^{16}}\right) \qquad (4)$$

This technique allows us to determine the electron density between 10^{14} and 10^{18} cm^{-3} [36]. N_e is the electronic density in cm^{-3} and w is the electronic impact parameter, which was obtained from [37,38]. Ionic broadening may be neglected here because it is much less than electronic broadening. The $\Delta\lambda_{stark}$ was obtained by means of the Lorentzian profile

deconvolution process using individually ionized titanium line at 454.9 nm and the instrumental broadening [39].

$$\Delta\lambda_{stark} = \Delta\lambda_{tot} - \Delta\lambda_{inst} \quad (5)$$

The instrumental broadening (0.53±0.02 nm), was measured using the FWHM at the second laser harmonic.

Table 1

Wavelength λ_{ki}, nm	Lower level	Upper level	$A_{ki}g_k$, s^{-1}	E_k, eV
430.00	$3d^3a^4P$	$3d^2(^3F)4pz^4D°$	1.30×10^8	4.0626
439.50	$3d^2(^1D)4sa^2D$	$3d^2(^3F)4pz^2F°$	7.50×10^7	3.9043
444.38	$3d^2(^1D)4sa^2D$	$3d^2(^3F)4pz^2F°$	6.48×10^7	3.8692
446.45	$3d^3a^2G$	$3d^2(^3F)4pz^2F°$	8.00×10^7	3.9043
448.83	$3d4s^2c^2D$	$3d^2(^1G)4px^2F°$	1.02×10^8	5.8851
450.13	$3d^3a^2G$	$3d^2(^3F)4pz^2F°$	5.62×10^7	3.8692
454.96	$3d^3a^2H$	$3d^2(^3F)4pz^2G°$	2.53×10^8	4.3082
457.20	$3d^3a^2H$	$3d^2(^3F)4pz^2G°$	1.54×10^8	4.2828

Figures 6a and 6b show the time-evolution of T_e and N_e at different RF powers. We observe a tendency to decrease in T_e and N_e with increasing power. However, the range of these variations is within the error bars and therefore, it is not possible to determine if it occurs due to the RF source. On the other hand, Figures 6c and 6d show the time-evolution of T_e and N_e at different nitrogen pressures. Here we observe that, with increasing pressure, both the density and the temperature decrease slowly. We attribute this to the plume confinement, since fast image analysis at low pressure shows that the plume expands rapidly, while at high pressure, the expansion is slowed down by collisions with the background gas.

The McWhirter criterion was used to validate whether the plasma is in LTE [40]

$$N_e(cm^{-3}) \geq 1.6x10^{12}T^{1/2}\Delta E^3 \,, \quad (6)$$

where T is the temperature (in kelvin) and ΔE is the energy difference between states (in electron-volts). The highest temperature value we obtained was approximately 2 eV. Hence

in our experiment, the criterion gives $N_e \geq 4.93\ x\ 10^{15} cm^{-3}$. Since, we measured an average density value of $1\ x\ 10^{17} cm^{-3}$, it can be assume that the plasma at 5 mm from the target is in LTE.

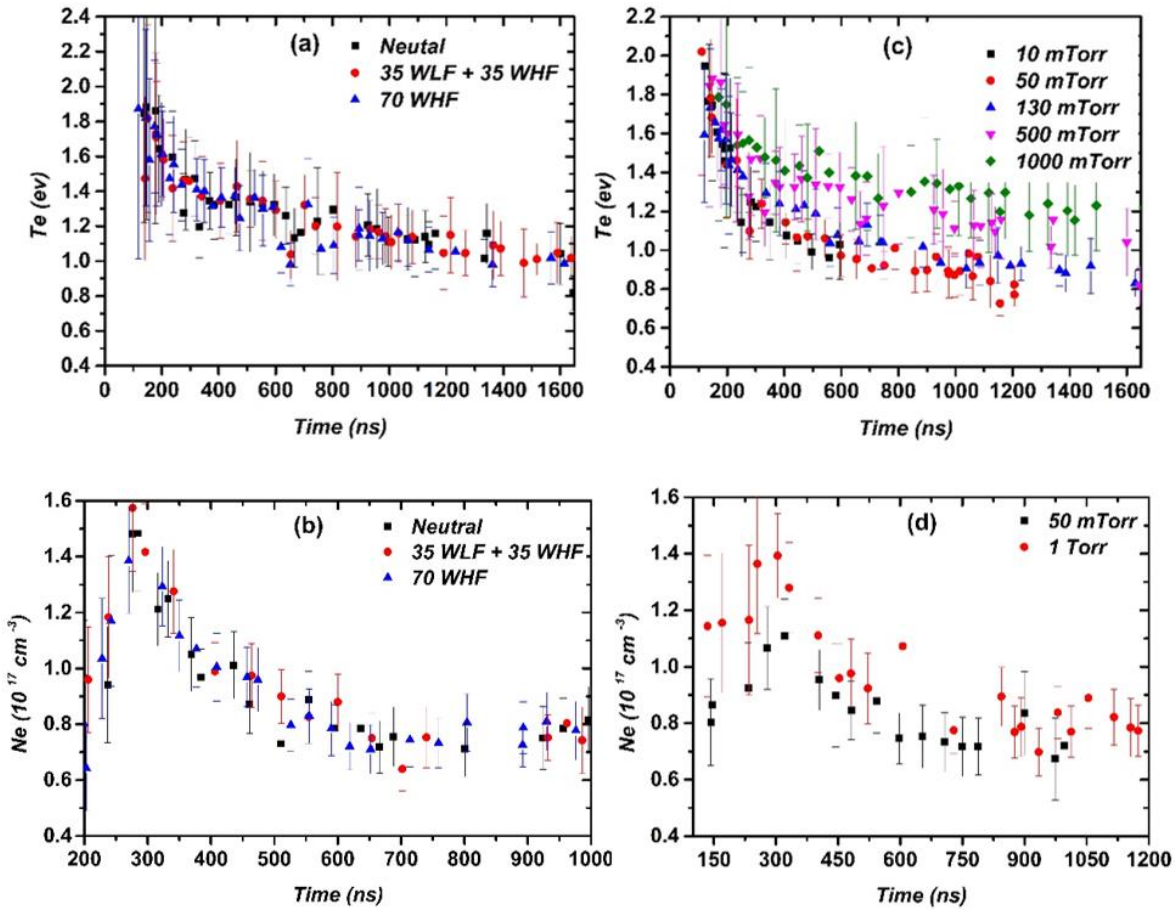

Figure 6. Temporal evolution of **a)** T_e and **b)** N_e at different RF power, **c)** T_e and **d)** N_e at different neutral pressure.

3.4. Interferometry

A Mach-Zehnder interferometer was used to obtain a two-dimensional plume density profile at early times. The phase shift is proportional to the line integral of density [39]:

$$\Delta\phi = \frac{e^2\lambda}{4\pi\varepsilon_o m_e c^2} \int N_e . dl \quad , \qquad (7)$$

where $\Delta\phi$ is the phase shift in fringe, λ is the laser probe wavelength and N_e is the electron density. Interferometric Data Evaluation Algorithms (IDEA) software was used to make the

two-dimensional map [41,42]. FFT analysis was employed from IDEA to extract the phase map, subtracted the background fringe, and calibrated in units of (cm^{-2}).

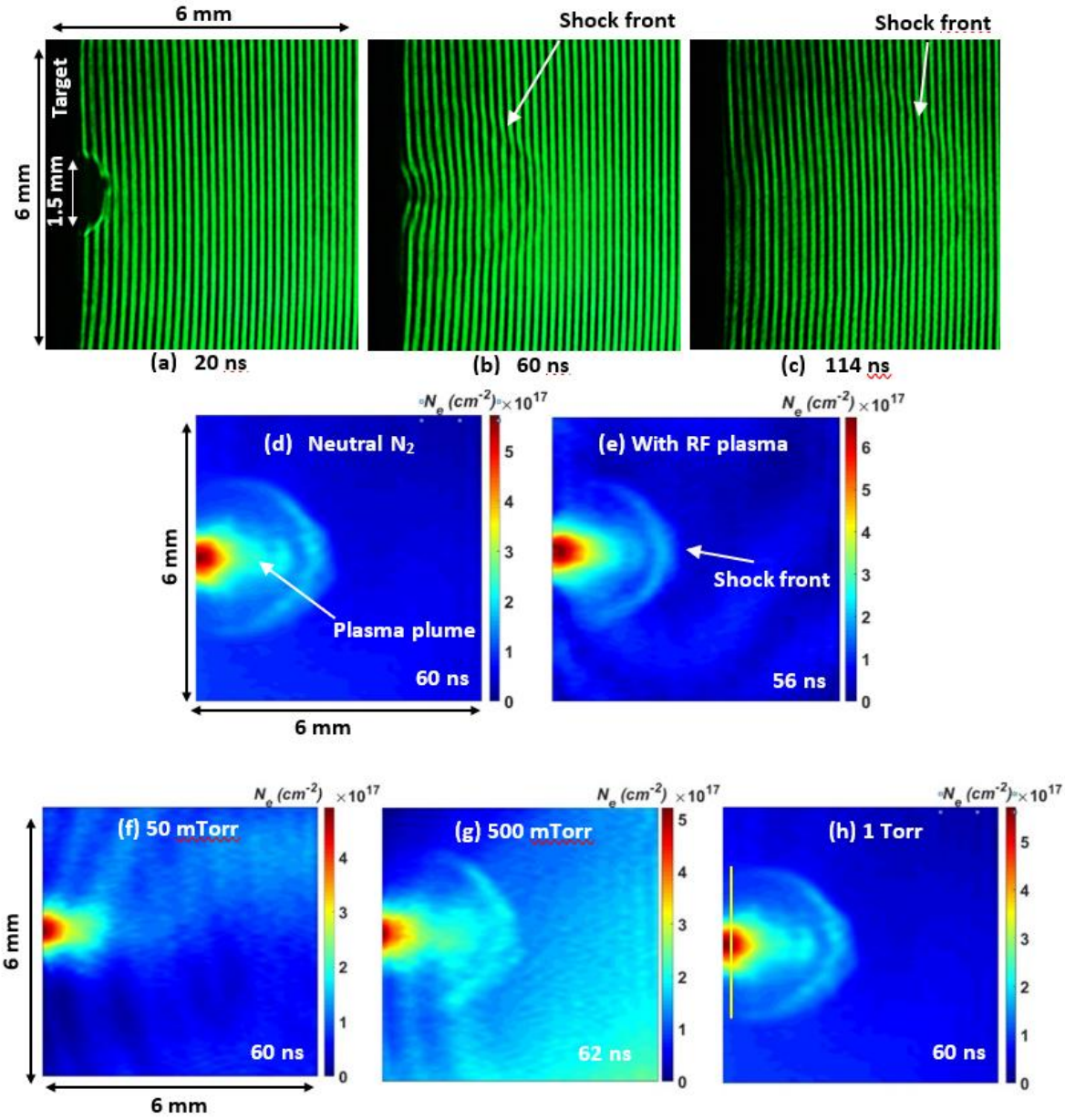

Figure 7. Optical interferograms of Ti expansion at 1 Torr of neutral nitrogen at different delay times of **a)** 20 ns, **b)** 60 ns, and **c)** 114 ns, **(d, e)** Show the 2D electronic density map obtained at 1 Torr of nitrogen without and with RF plasma (70 WHF), respectively. Figs. **(f,g,h)** show the 2D electronic density map at 50 mTorr, 500 mTorr and 1 Torr of neutral nitrogen, respectively.

Figures 7a, 7b, and 7c show a series of interferograms in 1 Torr of nitrogen at delays of 20 ns, 60 ns, and 114 ns, respectively. At 20 ns or less, a dark hemisphere is observed because at such early time the plasma density is too refractive. Later, at 114 ns, the plasma has expanded sufficiently and the fringe shift produced by the shock front is barely observable. The density N_e at this time is of the order of $10^{16} - 10^{17} cm^{-3}$, which agrees with the Stark broadening analysis. At 60 ns, the plasma has an intermediate density, which allows a good quality interferogram. Figures 7d and 7e show 2D electronic density map obtained at 1 Torr of nitrogen without and with RF plasma (70W HF), respectively. Shock front formation is observed due to the compression of background gas by the plasma plume expansion. No significant differences are observed between this pair of images. However, a slight variation in the plasma plume size, with well-defined boundaries, is observed in the presence of the background RF plasma. Figures 7f, 7g, 7h show the behavior of plasma plume at different neutral nitrogen pressure. Here it may be seen that, as the pressure increases, the size of the plasma plume decreases; hence it is denser due to the effect of confinement. Furthermore, a strong shock wave is observed at higher pressure due to the increase in the number of particles that are compressed by the plasma plume. In all cases, the electron density was calculated near the target, as indicated by a solid yellow line in figure 7h. On assuming the plasma to have cylindrical symmetry, the inverse Abel transform gives a maximum value for the titanium plasma density of 7.5 x10^{18} cm^{-3}.

3.5. Relevance to materials science

The results we have presented provide extensive information which is very relevant understand and optimize the process of growing thin films of TiN. The image analysis allows the measurement of maximum plume volume to be at 130 mTorr. Consequently, a larger area may be deposited on a nearby substrate but at a lower deposition rate. At lower pressures, the deposition rate could increase while the coverage area decreases because the expansion is mostly perpendicular to the surface. Furthermore, the adhesion to the substrate may well be greater due to free expansion with corresponding higher velocities. If the pressure is above 130 mTorr, the deposition rate may increase but the area covered decreases. However, the adhesion to the substrate will decrease due to the deceleration of the plasma by the drag effect. Again, the film roughness may well increase due to the appearance of small droplets

formed in the cooling process of the confined plasma. This is especially detrimental to possible optical applications. Optical spectroscopy highlights more relevant results of this work. We observe that increasing the nitrogen pressure increases the concentration of N II species. This favors the concentration of nitrogen in the deposited film [33]. However, as we have also discussed, increasing pressure could increase film roughness. On the other hand, we observe that high-frequency power increases the ion concentration due to the very rapid response of electrons at high frequencies which enhances excitation by electron-atom collision. This effect is useful since a higher concentration of nitrogen in the film can be obtained without affecting its roughness. Finally, interferometry allows spatial and temporal measurement of the plasma plume density and shock wave under different experimental conditions. Moreover, interferometry allows us to observe different dynamic structures that cannot be visualized by image analysis alone.

4. Conclusions

We have used a radio frequency discharge to study the effect of RF power on the composition and dynamics of the titanium plasma plume formed in a PE-PLD system with nitrogen at different background pressures. We have combined three different non-invasive techniques to complete a coherent study. From the fast image analysis, information on the velocity and morphology was obtained for different pressure values and RF power. In addition, the information from the images allows us to distinguish the region of the plasma where the spectra were taken, which in turn allows an improved interpretation of the evolution of the plasma density and temperature.

The principal difference between the PLD and PE-PLD system is observed in the emission spectra analysis, where an increase in the background reactivity is shown to be the case. In a nitrogen background an increase in the N II line (460.1 nm) was observed with increasing frequency. Furthermore, a decrease in the Ti II line (454.9 nm) was observed with increasing power. This allows the conclusion that, by increasing the background reactivity, titanium may either recombine with the background RF plasma species or make transitions to another energy level due to changes in the plasma parameters. With increasing pressure, the effect of confinement affects the velocity of the plume and in consequence the cooling rate and density of the plasma. In addition it was observed that, with increasing pressure, the

intensity of the Ti II (454.9 nm) and N II (460.1 nm) lines increase due to increased collisionality. Finally, a denser shock wave is observed with increasing pressure.

The plasma parameters and characteristics of this study contribute to the understanding of both basic plasma physics and applications in thin film deposition by PE-PLD. A consequence of this is that it is expected that the increase in ionic species of Ti, and N, due to the enhanced collisionality, will improve the deposition and chemical bonding of titanium alloys. Future research in hand will study the effects of these differences in dynamics and composition in the growth of TiN thin films.

Acknowledgements

This work is funded by FONDECYT project 1170261 and ANID/Scholarship Program/ doctorado nacional/2018 – 21181050. MF acknowledges FONDECYT 1180100.

References

1. Giardini, A., Marotta, V., Orlando, S., & Parisi, G. P. Titanium nitride thin films deposited by reactive pulsed-laser ablation in RF plasma. *Surf. Coat. Technol.* ***151***, 316-319, https://doi.org/10.1016/S0257-8972(01)01563-8 (2002).
2. Teghil, R. *et al*. Femtosecond pulsed laser ablation and deposition of titanium carbide. *Thin Solid Films* ***515***(4), 1411-1418, https://doi.org/10.1016/j.tsf.2006.03.057 (2006).
3. Gence, L. *et al*. Wrinkled titanium nitride nanocomposite for robust bendable electrodes. *Nanotechnology* ***30***(49), 495705, https://doi.org/10.1088/1361-6528/ab416c (2019).
4. Suda, Y., Kawasaki, H., Doi, K., Nanba, J., & Ohshima, T. Preparation of crystalline TiC thin films grown by pulsed Nd: YAG laser deposition using Ti target in methane gas. *Mater. Charact.* ***48***(2-3), 221-228, https://doi.org/10.1016/S1044-5803(02)00243-7 (2002).
5. Nunes Kirchner, C. *et al*. Evaluation of thin film titanium nitride electrodes for electroanalytical applications. *Electroanalysis: An International Journal Devoted to Fundamental and Practical Aspects of Electroanalysis*, ***19***(10), 1023-1031, https://doi.org/10.1002/elan.200703832 (2007).
6. Subramanian, B., Muraleedharan, C. V., Ananthakumar, R., & Jayachandran, M. A comparative study of titanium nitride (TiN), titanium oxy nitride (TiON) and titanium aluminum nitride (TiAlN), as surface coatings for bio implants. *Surf. Coat. Technol.* **205**(21-22), 5014-5020, https://doi.org/10.1016/j.surfcoat.2011.05.004 (2011).
7. Chin, Y. L. *et al*. Titanium nitride membrane application to extended gate field effect transistor pH sensor using VLSI technology. *Jpn. J. Appl. Phys*. **40**(11R), 6311, https://doi.org/10.1143/JJAP.40.6311 (2001).
8. Saikia, P. *et al*. Effect of hydrogen addition on the deposition of titanium nitride thin films in nitrogen added argon magnetron plasma. *J. Phys. D: Appl. Phys*. **49**(22), 225203, https://doi.org/10.1088/0022-3727/49/22/225203 (2016).
9. Cisternas, M., Mellero, F., Favre, M., Bhuyan, H., & Wyndham, E. TiN coatings on titanium substrates using plasma assisted ion implantation. *J. Phys.: Conf. Ser.* **591**, 012043. IOP Publishing, https://doi.org/10.1088/1742-6596/591/1/012043 (2015).
10. Chaudhry, A. U., Mansoor, B., Mungole, T., Ayoub, G., & Field, D. P. Corrosion mechanism in PVD deposited nano-scale titanium nitride thin film with intercalated titanium for protecting the surface of silicon. *Electrochimica Acta*, *264*, 69-82. https://doi.org/10.1016/j.electacta.2018.01.042. (2018)
11. Cheng, H. E., & Wen, Y. W. Correlation between process parameters, microstructure and hardness of titanium nitride films by chemical vapor deposition. *Surface and Coatings Technology*, *179*(1), 103-109. https://doi.org/10.1016/S0257-8972(03)00789-8 (2004).
12. Major, B., Mróz, W., Wierzchoń, T., Waldhauser, W., Lackner, J., & Ebner, R. (2004). Pulsed laser deposition of advanced titanium nitride thin layers. Surface and Coatings Technology, 180, 580-584. https://doi.org/10.1016/j.surfcoat.2003.10.154 (2004)

13. Capitelli, M., Casavola, A., Colonna, G., & De Giacomo, A. Laser-induced plasma expansion: theoretical and experimental aspects. *Spectrochim. Acta, Part B* **59**(3), 271-289, https://doi.org/10.1016/j.sab.2003.12.017 (2004).

14. Schou, J. Physical aspects of the pulsed laser deposition technique: The stoichiometric transfer of material from target to film. *Applied Surface Science*, *255*(10), 5191-5198. https://doi.org/10.1016/j.apsusc.2008.10.101 (2009).

15. Blank, D. H., Dekkers, M., & Rijnders, G. Pulsed laser deposition in Twente: from research tool towards industrial deposition. Journal of physics D: applied physics, 47(3), 034006. https://doi/10.1088/0022-3727/47/3/034006 (2013).

16. Eason, R. (Ed.). Pulsed laser deposition of thin films: applications-led growth of functional materials. John Wiley & Sons. (2007).

17. Rossall, A. K., van den Berg, J. A., Meehan, D., Rajendiran, S., & Wagenaars, E. Analysis of plasma enhanced pulsed laser deposition of transition metal oxide thin films using medium energy ion scattering. *Nucl. Instrum. Methods Phys. Res., Sect. B* **450**, 274-278, https://doi.org/10.1016/j.nimb.2018.06.023 (2019).

18. Chou, C. M., Lai, C. C., Chang, C. W., Wen, K. H., & Hsiao, V. K. Radio-frequency oxygen-plasma-enhanced pulsed laser deposition of IGZO films. *AIP Advances* **7**(7), 075309, https://doi.org/10.1063/1.4994677 (2017).

19. Rajendiran, S., Meehan, D., & Wagenaars, E. Plasma-Enhanced Pulsed Laser Deposition of copper oxide and zinc oxide thin films. *AIP Advances*. https://doi.org/10.1063/5.0008938 (2020).

20. Bourquard, F. *et al*. Effect of nitrogen surrounding gas and plasma assistance on nitrogen incorporation in aC: N films by femtosecond pulsed laser deposition. *Appl. Surf. Sci.* **374**, 104-111, https://doi.org/10.1016/j.apsusc.2015.10.039 (2016).

21. Geohegan, D. B., Chrisey, D. B., & Hubler, G. K. *Pulsed Laser Deposition of Thin Films*. (eds. Chrisey and GK Hubler), Wiely, New York, 59-69. (1994).

22. Saikia, P. *et al*. Experimental investigations of the effect of the neutral gas pressure on the separate control of ion energy and flux in dual frequency capacitively coupled plasmas. *Phys. Plasmas* **26**(8), 083505, https://doi.org/10.1063/1.5094603 (2019).

23. Saikia, P. *et al*. Study of dual radio frequency capacitively coupled plasma: an analytical treatment matched to an experiment. *Plasma Sources Sci. Technol.* **27**(1), 015014, https://doi.org/10.1088/1361-6595/aaa565 (2018).

24. Saikia, P. *et al*. A nonlinear global model of single frequency capacitively coupled plasma and its experimental validation. *AIP Advances* **8**(4), 045113, https://doi.org/10.1063/1.5022654 (2018).

25. Harilal, S. S. *et al*. Plume splitting and sharpening in laser-produced aluminium plasma. Phys. D: Appl. Phys **35**(22), 2935 (2002).

26. Harilal, S. S. *et al*. Internal structure and expansion dynamics of laser ablation plumes into ambient gases. *J. Appl. Phys,* **93**(5), 2380-2388. https://doi.org/10.1063/1.1544070 (2003).

27. Sankar, P *et al*. Optical emission and dynamics of aluminum plasmas produced by ultrashort and short laser pulses. *J. Anal. At. Spectrom*. **32**(6), 1177-1185. https:// doi.org/ 10.1039/c7ja00133a (2017).

28. Chapman, S., Cowling, T. G., & Burnett, D. *The Mathematical Theory of Non-Uniform Gases: An Account of The Kinetic Theory of Viscosity, Thermal Conduction and Diffusion in Gases*. (Cambridge university press 1990).

29. Shu, F. H. *The Physics of Astrophysics: Gas Dynamics* (Vol. 2) (University Science Books 1991).

30. Geohegan, D. B. Fast intensified- CCD photography of YBa2Cu3O7− x laser ablation in vacuum and ambient oxygen.*Appl. Phys. Lett.* **60**(22), 2732-2734, https://doi.org/10.1063/1.106859 (1992).

31. NIST Atomic Spectra Database. https://www.nist.gov/pml/atomic-spectra-database (2019).

32. Godyak, V. A., Piejak, R. B., & Alexandrovich, B. M. Effective electron collision frequency and electrical conductivity of radio frequency plasmas. *J. Appl. Phys*. **85**(6), 3081-3083, https://doi.org/10.1063/1.369646 (1999).

33. Escalona, M. *et al*. Study of titanium nitride film growth by plasma enhanced pulsed laser deposition at different experimental conditions. *Surf. Coat. Technol.*, 126492, https://doi.org/10.1016/j.surfcoat.2020.126492 (2020).

34. Boulmer-Leborgne, C., Hermann, J., & Dubreuil, B. Plasma formation resulting from the interaction of a laser beam with a solid metal target in an ambient gas. *Plasma Sources Sci. Technol.* **2**(3), 219, https://doi.org/10.1088/0963-0252/2/3/013 (1993).

35. Hermann, J., Boulmer- Leborgne, C., Mihailescu, I. N., & Dubreuil, B. Multistage plasma initiation process by pulsed CO2 laser irradiation of a Ti sample in an ambient gas (He, Ar, or N2). *J. Appl. Phys* **73**(3), 1091-1099, https://doi.org/10.1063/1.353271 (1993).

36. Griem H.R., *Principles of Plasma Spectroscopy* (Cambridge University Press, Cambridge, 1997).

37. Manrique, J., Aguilera, J. A., & Aragon, C. Experimental Stark widths and shifts of Ti II spectral lines. *Mon. Not. R. Astron. Soc.* ***462***(2), 1501-1507, https://doi.org/10.1093/mnras/stw1641 (2016).

38. Tankosić, D., Popović, L. Č., & Dimitrijević, M. S. Electron-impact Stark broadening parameters for Ti II and Ti III spectral lines. *At. Data Nucl. Data Tables* **77**(2), 277-310, https://doi.org/10.1006/adnd.2000.0856 (2001).

39. Hutchinson, I. H. *Principles of Plasma Diagnostics* (Cambridge University 2002).

40. McWhirter R.W.P., Huddlestone R.H., Leonard, S.L. *Spectral intensities in Plasma Diagnostic Techniques*, (Academic Press 1965).

41. Hipp, M. *et al*. Application of interferometric fringe evaluation software at Technical University Graz. In *Interferometry'99: Applications* (**Vol. 3745**, pp. 281-292). *International Society for Optics and Photonics*, https://doi.org/10.1117/12.357789 (1999).

42. Hipp, M., & Reiterer, P. *User Manual for IDEA 1.7.* (Institut für Experimental Physik) http://optics.tu-graz.ac.at/idea/Manual_IDEAv17.pdf (2003).